

Tracing Magnetic Field Morphology Using the Velocity Gradient Technique in the Presence of CO Self-absorption

Cheng-han Hsieh¹, Yue Hu^{2,3}, Shih-Ping Lai^{1,4}, Ka Ho Yuen², Sheng-Yuan Liu⁴, I-Ta Hsieh⁴, Ka Wai Ho⁵, and A. Lazarian²

Department of Physics, National Tsing Hua University, Taiwan

Department of Astronomy, University of Wisconsin–Madison, USA; lazarian@astro.wisc.edu

Department of Physics, University of Wisconsin–Madison, USA

Institute of Astronomy of Astrophysics, Academia Sincia, Taiwan

Chinese University of Hong Kong, Hong Kong

Received 2018 September 25; revised 2019 January 8; accepted 2019 January 29; published 2019 February 28

Abstract

Probing magnetic fields in self-gravitating molecular clouds is generally difficult, even with the use of polarimetry. Based on the properties of magnetohydrodynamic turbulence and turbulent reconnection, the velocity gradient technique (VGT) provides a new way of tracing magnetic field orientation and strength based on spectroscopic data. Our study tests the applicability of VGT in various molecular tracers, e.g., ¹²CO, ¹³CO, and C¹⁸O. By inspecting synthetic molecular-line maps of CO isotopologs generated through radiative transfer calculations, we show that the VGT can be successfully applied in probing the magnetic field direction in the diffuse interstellar medium, as well as in self-gravitating molecular clouds.

Key words: ISM: magnetic fields – ISM: molecules – magnetohydrodynamics (MHD) – methods: numerical – radiative transfer – turbulence

1. Introduction

Magnetized turbulence is of great importance in many astrophysical processes in the interstellar medium (ISM), especially in the stage of cloud formation and evolution (McKee & Ostriker 1977; Audit & Hennebelle 2005; Crutcher 2012). However, the study of magnetic fields in the ISM is complicated, since the ISM has multiple phases where the levels of ionization, temperature, density, and molecular abundance change drastically (Falgarone & Passot 2003). The most common techniques to study magnetic fields are stellar light polarization, emission from aligned grains (Andersson et al. 2015), and molecular-line splitting (Zeeman effect; Crutcher et al. 2010). By measuring the polarization from stars (Heiles 2000), one can get some insight into the morphology of the galactic magnetic field. However, as it is only possible to sample magnetic fields in the direction toward stars with known distances, this way of magnetic field sampling is limited. Dust polarization measurements, on the other hand, determine the direction of the projected magnetic field. They can also be used within the Davis-Chandrasekhar-Fermi technique to roughly estimate the plane-of-sky averaged magnetic field strength (Davis 1951; Chandrasekhar & Fermi 1953; Falceta-Gonçalves et al. 2008). Unfortunately, the measurement of the magnetic field through dust polarization is in general difficult, since the grain alignment efficiency drops significantly in the case of high optical depth, which limits the reliability of tracing the magnetic field in optically thick regions (Andersson et al. 2015). Line splitting, such as the Zeeman effect, directly measures the intensity of the line-of-sight magnetic field (Crutcher & Troland 2008; Crutcher et al. 2010) without any assumptions. The Zeeman splitting is a small fraction of the line width, and only the Stokes spectra can be detected; these spectra reveal the sign and magnitude of the line-of-sight component of the magnetic field (Troland & Crutcher 2008). However, the Zeeman measurements require very high sensitivity and long integration times. Thus, in many cases,

only the upper limits of the magnetic field strength can be obtained.

The velocity gradient technique (VGT; González-Casanova & Lazarian 2017; González-Casanova et al. 2017; Yuen & Lazarian 2017a, 2017b; Lazarian & Yuen 2018b) is a new technique that can measure the direction and intensity of the magnetic fields using only spectroscopic observations. The VGT has its foundations in the theory of MHD turbulence, which states that the velocity motions of turbulent fluids are anisotropic and the direction of anisotropy is determined by the local direction of the magnetic field; i.e., fluid motions in the presence of MHD turbulence are eddy-like, and the axis of rotation is aligned with the magnetic field surrounding the eddy (Goldreich & Sridhar 1995; Lazarian & Vishniac 1999). This property of turbulent motion follows from the theory of turbulent reconnection (Lazarian & Vishniac 1999). This theory predicts that magnetic fields do not present an impediment for eddies that are aligned with the magnetic field surrounding them. Therefore, most of the energy of the turbulent cascade is channeled into these types of eddies that trace the magnetic field direction. It is essential for the VGT that the alignment of the eddies happens with the local magnetic field direction, rather than the mean of the magnetic field direction. Incidentally, the original theory in Goldreich & Sridhar (1995) does not make this distinction. The fact that the local system of reference should be used is obvious from the turbulent reconnection theory (Lazarian & Vishniac 1999) and is proved reliably in numerical simulations (Cho & Vishniac 2000; Maron & Goldreich 2001; Cho et al. 2002). Due to the fact that eddies trace the local direction of the magnetic field,

The theory of turbulent reconnection predicts the violation of the accepted concept of flux freezing in turbulent conducting fluids (see more in Eyink et al. 2011, 2013), which has important consequences for star formation (Lazarian et al. 2012).

⁷ Formally, the Goldreich & Sridhar theory is formulated in the mean field of reference where the Goldreich & Sridhar crucial balance relations, which are the cornerstone of the theory, are not valid.

the VGT captures the detailed magnetic field structure within the turbulent volume under study.

The VGT was first applied to HI data (Yuen & Lazarian 2017a) and then extended to the cases where gravity (Yuen & Lazarian 2017b) and self-absorption (González-Casanova et al. 2017) are important. Yuen & Lazarian (2017b) presented a new smoothing method to estimate the gradients that presents a more reliable estimation, in which the VGT has still been used to measure the magnetic field direction in HI and ¹³CO. In its original formulation (see González-Casanova & Lazarian 2017), the VGT used centroids as the observationally available proxy of the velocity distribution. Later, in Lazarian & Yuen (2018b), it was proposed to trace magnetic fields using gradients of intensity within the thin channel maps, i.e., using the velocity channel gradients (VChGs). This is possible, as the theory of the nonlinear mapping of motions from a turbulent volume to the position-position-velocity (PPV) space (Lazarian & Pogosyan 2000) predicts that thin channel maps represent the velocity statistics well. The VChG approach shows higher accuracy compared to the analysis based on centroids. It also increases the utility of the VGT, as the per-channel gradient analysis allows observers to distinguish molecular clouds along the line of sight in the galactic plane, as well as to obtain the 3D magnetic field tomography of HI using the galactic rotation curve (Gonzalez-Casanova & Lazarian 2018).

In parallel with the VGT, we also use its derivative technique, namely, intensity gradients (IGs). The IG technique should be distinguished from the histograms of relative orientation (HRO) technique proposed in Soler et al. (2013). Within the IG approach (see Yuen & Lazarian 2017b), one uses the procedures developed within the VGT technique, e.g., the block-averaging procedure, in order to reliably determine the gradient directions that can be compared to the magnetic field direction on a point-wise basis. In HRO, on the contrary, no point-wise comparison is possible; only the comparison in terms of the statistics of the orientations as a function of column density is available. In general, density fluctuations are less-direct statistics of turbulence compared to velocities (see Cho & Lazarian 2003), and therefore we expect less accurate magnetic field tracing with IGs compared to that available with the VGT. The synergy of using the IGs and velocity gradients is discussed elsewhere.

Depending on the physical scale of the observations, self-gravity can strongly affect the dynamics of the gas in giant molecular clouds (GMCs). The GMCs are studied through molecular transitions, most commonly those of ¹²CO, ¹³CO, and C¹⁸O. It is therefore important to understand the effects of self-gravity using molecular PPV data in the VGT. This work then builds on the separate studies of self-gravity and molecular emission in PPV data cubes. In this work, we apply the VGT to analyze two conditions, with and without self-gravity. By processing the ideal MHD simulations with a new radiative transfer code, the Simulation Package for Astronomical Radiative Xfer (SPARX), we produce synthetic maps of ¹²CO, ¹³CO, and C¹⁸O.

These tracers are most prevailing in the diffuse ISM, and the differences in optical depths between these tracers could offer information on the magnetic field along the line of sight.

In what follows, in Section 2, we discuss how the VGT performs and is optimized in the case of self-absorbing, self-gravitating molecular tracer maps. In Section 3, we give a brief

view of the MHD simulation and the radiative transfer calculation. In Section 4, we present our results about the VGT in the presence of self-absorbing media and self-gravity. In Section 5, we discuss the influence of radiative transfer in the VGT. In Section 6, we give our conclusions.

2. The Theoretical Expectation of the VGT under Different Molecular Tracer Maps

2.1. VGT

The development of the VGT is highly related to the recent establishment of MHD turbulence theory through numerical studies. The core theoretical consideration is derived from Goldreich & Sridhar (1995) and Lazarian & Vishniac (1999). Goldreich & Sridhar (1995, hereafter GS95) predicted the anisotropy of MHD turbulence, and Lazarian & Vishniac (1999) introduced the theory of turbulent reconnection. Lazarian & Vishniac (1999) showed that magnetic field lines are allowed to rotate perpendicularly around each other due to fast turbulent reconnection. Similarly, in the framework of turbulence, the turbulent eddies are not constrained from rotating perpendicular to the direction of the magnetic field. As a result, in random turbulence driving, eddy motions perpendicular to the magnetic field lines become more probable, since the magnetic tension force resists any other type of magnetic field motion.

Incidentally, it raises the consideration of the importance of the local magnetic field in respect to the motions of Alfvénic turbulence. The concept of the local system of reference was confirmed in Cho & Vishniac (2000). Alfvénic eddies that are not constrained by magnetic tension create a Kolmogorov cascade with velocities $v_l \sim l_{\perp}^{\frac{1}{3}}$, where l_{\perp} is measured with respect to the local direction of the magnetic field. It is evident that the eddies mixing magnetic field lines perpendicular to their direction should induce Alfvénic waves along the magnetic field. Hence, it is essential for the VGT to trace the local magnetic field around turbulent eddies, rather than the mean magnetic field.

It is a well-established fact that the statistics of Alfvénic turbulence is anisotropic along the local magnetic field directions (Lazarian & Vishniac 1999; Cho et al. 2002). Similarly, the velocity gradients also show a distribution of directions in which the most probable orientation of gradients is perpendicular to the magnetic field direction (Yuen & Lazarian 2017a). Hence, the direction of the magnetic field can be obtained by rotating the most probable orientation of gradients by 90°.

In the framework of the VGT, three types of 2D maps are frequently used to trace magnetic fields in a number of contexts: intensity maps I(x, y), velocity centroid maps C(x, y), and velocity channel maps Ch(x, y). These maps are produced by doing an integral along the velocity axis of the PPV cube for all tracers. In this work, we use I(x, y) and C(x, y):

$$C(x, y) = \frac{\int dv \ \rho(x, y, v) \cdot v}{I(x, y)}, \tag{1}$$

$$I(x, y) = \int dv \ \rho(x, y, v), \tag{2}$$

where ρ is the PPV gas density, and v is the velocity component along the line of sight.

Table 1
Description of the MHD Simulation Cubes

Model	M_S	M_{A}	$\beta = 2M_{\rm A}^2/M_{\rm S}^2$	¹² CO, IGs	¹³ CO, IGs	C ¹⁸ O, IGs	¹² CO, VCGs	¹³ CO, VCGs	C ¹⁸ O, VCGs
b11	0.41	0.04	0.02	34 30	36 32	43 30	33 35	33 38	35 38
b12	0.92	0.09	0.02	15 10	19 11	25 16	14 16	16 18	18 25
b13	1.95	0.18	0.02	7 5	10 7	17 11	77	10 8	17 12
b14	3.88	0.35	0.02	10 8	10 11	20 17	10 9	12 12	16 16
b15	7.14	0.66	0.02	NA 18	NA 19	NA 28	NA 20	NA 21	NA 27
b21	0.47	0.15	0.2178	28 29	30 33	39 35	22 26	29 29	35 30
b22	0.98	0.32	0.2178	18 15	30 25	31 33	19 18	22 24	24 29
b23	1.92	0.59	0.2178	14 14	19 20	22 29	14 15	18 21	22 20
b31	0.48	0.48	2	33 37	68 61	66 61	37 38	36 39	37 36
b32	0.93	0.94	2	30 29	42 46	43 41	31 35	43 36	46 34
b41	0.16	0.49	18.3654	55 57	59 57	57 56	50 45	53 45	51 45
b42	0.34	1.11	18.3654	36 40	53 48	54 52	41 39	46 50	44 51
b51	0.05	0.52	200	59 58	58 56	58 57	54 54	54 54	53 55
b52	0.10	1.08	200	64 69	64 67	64 67	47 48	47 48	46 49

Notes. Each MHD cube contains three types of absorbing media, 12 CO, 13 CO, and 18 O, with emission line J=1-0. Both the ideal case without self-gravity and the case with the presence of self-gravity are considered. The resolution of each cube is 480^3 . The last six columns show the relative angles for the IG and VCG methods such that under the 68.27% confidence interval (1σ), the VGT predictions are the same as the simulated B field. Inside each cell, the first values show the results for self-gravity data, and the second values show the results for cases without self-gravity. Here M_s and M_A are the instantaneous values at each snapshot taken.

•

Then, the gradient angle at pixel (x_i, y_i) is defined as

$$\nabla_{i,j} = \tan^{-1} \left[\frac{f(x_i, y_{j+1}) - f(x_i, y_j)}{f(x_{i+1}, y_j) - f(x_i, y_j)} \right], \tag{3}$$

where f(x, y) can be either I(x, y) or C(x, y). This will make up the pixelized gradient field of the spectroscopic data.

Yuen & Lazarian (2017a) proposed the recipe of sub-block averaging to predict the direction of the magnetic field through gradients in a statistical region of interest. When the statistical samples are sufficiently large (Yuen & Lazarian 2017a and, later, Lazarian & Yuen 2018b provided a criterion to determine the optimal block size for a given number of gradient statistics), the histogram of gradient orientations will show a Gaussian profile. Within a block, we obtained the most probable orientation, which is the peak of the Gaussian corresponding to the local direction of the magnetic field within the block. The VGT uses the sub-block-averaging method, and it is getting results that are very different from those that can be obtained with the HRO technique (Soler et al. 2013; Soler & Hennebelle 2017). The latter technique uses gradients of intensity, and it requires polarimetry data to define the direction of the magnetic field, while the VGT is a polarization-independent and complementary way of finding the magnetic field direction.

2.2. The Effect of Radiative Transfer

It has already been demonstrated that the prediction of the magnetic field from the VGT shows good alignment with the presence of absorbing media 13 CO J=2-1 (González-Casanova et al. 2017). Aside from 13 CO, 12 CO and 18 O are also common tracers of interstellar molecular flows when the number density of neutral hydrogen (H I) is between 10^2 and 10^4 cm⁻³, which is the common density for newly born self-gravitating molecular clouds (Crutcher 2012). The most important difference between the isotopologs of CO in tracing the molecular flow is their optical depths. That means one can

use ¹²CO to trace the flow of molecular gases in the diffuse surrounding region of a self-gravitating molecular cloud due to its weaker penetration power while using ¹³CO and C¹⁸O to estimate the accumulated contribution of gas motions in a thicker line-of-sight cloud.

Due to the differences in optical depths of CO isotopologs, it is possible to use the VGT to stack the 3D tomography from surrounding layers to deeper core layers. However, it is difficult to explore the magnetic field morphology through the VGT when strong self-gravity is present, since Yuen & Lazarian (2017b) and Lazarian & Yuen (2018b) suggested that the gradients of intensities and centroids are gradually rotating from $\perp B$ to $\parallel B$ when the stage of collapse increases. The separation of diffuse and dense media through molecular tracer maps with different optical maps assists observers in studying the velocity anisotropy and thus magnetic field structure of the molecular cloud from the outermost diffuse layer to the dense core layer.

3. Method

3.1. MHD Data

The numerical 3D MHD simulations are obtained from the code ZEUS-MP/3D (Hayes et al. 2006) with a single fluid, operator-split, staggered-grid MHD Eulerian assumption. The data have been used in Hu et al. (2018a) and Lazarian et al. (2018) to set up a 3D, uniform, isothermal turbulent medium.

Periodic boundary conditions, as well as solenoidal turbulence injections, are applied in the simulation for emulating a part of the interstellar cloud. We employ various Alfvénic Mach numbers $M_A = \frac{V_L}{V_A}$ and sonic Mach numbers in our simulation $M_S = \frac{V_L}{V_S}$, where V_L is the injection velocity, while V_A and V_S are the Alfvén and sonic velocities, respectively (see Table 1 for details.). We shall refer to the simulations of Table 1 by their model names. For instance, our figures will

have the model name indicating which data cube was used to plot the figure. The simulations are named with respect to a variation of the ascending values of β . The ranges of M_S , M_A , and β are selected so that they cover the different possible scenarios of astrophysical turbulence from very subsonic to supersonic cases. For each cube, we consider cases both with and without self-gravity in this work.

3.2. The Radiative Transfer Calculation

We performed 3D local thermal equilibrium (LTE) radiative transfer on a Cartesian grid to generate synthetic maps with the SPARX code. The SPARX code is designed to calculate radiative transfer for both molecular-line transitions and the dust continuum, and the details of the package are given in Appendix A.

In the calculation, molecular gas density and velocity information is extracted from the MHD data mentioned in Section 3.1. A gas temperature of 10 K, which is typical in molecular clouds (Wilson et al. 1997), is assumed. The fractional abundances of the CO isotopologs $^{12}\text{CO},^{13}\text{CO}$, and C¹⁸O are set to be $1\times10^{-4},\ 2\times10^{-6},\ \text{and}\ 1.7\times10^{-7},\ \text{respectively}.$ The commonly used $^{12}\text{CO-to-H}_2$ ratio of 1×10^{-4} comes from the cosmic value of C/H = 3×10^{-4} and the assumption that 15% of C is in the molecular form. For the abundance of ^{13}CO , we adopted a $^{13}\text{CO}/^{12}\text{CO}$ ratio of 1/69 (Wilson 1999). Hence, the $^{13}\text{CO-to-H}_2$ ratio is approximated to $2\times10^{-6}.$ With $^{12}\text{O}/^{18}\text{O}=500$ (Wilson et al. 2016), we obtain a C¹⁸O-to-H₂ ratio of $1.7\times10^{-7}.$

When producing the synthetic molecular channel maps, we focus on the lowest-transition J=1-0 of the CO isotopologs, in which the LTE condition is satisfied. The required (critical) density for thermally populating the J=1-0 of CO isotopologs is $\sim 10^3$ cm⁻³, which is comparable to the molecular gas density in the diffuse ISM. The high optical depth of the 12 CO J=1-0 transition further facilitates the reduction of the required (critical density) for the LTE population.

When applying the LTE assumption to ¹³CO on cloud models, factor of 2 uncertainties on the column density derived should be expected (van Dishoeck et al. 1992). For C¹⁸O, the molecular line is optically thinner than the other two species, allowing the tracer to trace into the denser regions of the clouds.

4. Responses from Different Optical Tracers

4.1. Effects of Self-gravity

After carrying out radiative transfer simulations for each model with SPARX, we produce different PPV data cubes for different tracers. We then compute integrated intensity maps (moment 0) and velocity centroid maps (moment 1) for each PPV cube (see Section 3 for more data details). After obtaining the moment maps, we then apply the VGT recipe (Yuen & Lazarian 2017a, 2017b; Lazarian & Yuen 2018b) to obtain q the prediction of B-field orientations. The recipe consists of the gradient operators, sub-block averaging (Yuen & Lazarian 2017a), and the error estimation method (Lazarian & Yuen 2018b). Inside each box, we collect all of the directions predicted by the gradients and use a shifted Gaussian function (Lazarian et al. 2018) to fit. In principle, the Gaussian profile with a shifting term is a better representation of the gradient orientation distribution in numerical simulations, since the

angle-independent shifting term is usually much higher than zero. For instance, with $M_A \sim 0.2$, the velocity isocontour axis ratio can be in hundreds (Xu & Lazarian 2018). However, simulations nowadays have limited resolution. There is a natural tendency for velocity contours to have smaller axis ratios due to the unresolvable minor axis. As a result, the count away from the peak of gradient orientation distribution would not be close to zero. A constant shift would address the issue of finite length. In practice, the shift will not change the prediction of peak location by block averaging. We set a criterion on such that if the random area (shifted region) is greater than the Gaussian area, then that block will not give predictions. We select a box size of 40² pixels for the Gaussian fitting process, meaning that the sub-block-averaged direction is given by the peak of the Gaussian fitting function on the gradient orientation histograms obtained from the 40×40 block.

The average value from the Gaussian fitting will be used to represent the VGT predictions in that box. The block-averaged vectors are then rotated 90° to indicate the direction of the magnetic field as predicted by the VGT. We plot the ¹²CO results for models b12, b13, b51, and b52 in Figures 1–4, respectively. As for the results of ¹³CO, C¹⁸O are shown in Appendix B (Figure 9) and Appendix C (Figure 10), respectively. In the simulations, we have 3D data on the magnetic fields. By mimicking dust polarization, we calculated the density-weighted averaged B fields in the plane of the sky and then compared these with VGT predictions to obtain a relative angle. To allow better comparison, we collect all the relative angles between the VGT predictions and simulated magnetic fields and present the results as cumulative plots.

Figures 1 and 2 are two examples showing that the VGT works very well. Here IG means that the gradient is computed from a moment 0 map, and velocity centroid gradient (VCG) means that the gradient is calculated from a moment 1 map. In Figure 2, we can see that the normalized cumulative counts quickly increase to above 0.9 within 20° relative angle. This means that 90% of the VGT-predicted B-field vectors in these models have relative angles less than 20°. As for b51 and b52 in Figures 3 and 4, the normalized cumulative counts are close to a random distribution. As later shown in Figure 5, these models fall close to the random distribution line. A random distribution of the cumulative relative-angle orientation histogram would indicate that the VGT fails to provide a reliable prediction of the magnetic field direction in the region of interest.

In order to compare the performance of the VGT across models, we define a parameter to determine whether the predictions are reliable. From each cumulative plot, we found the relative angle between VGT predictions and simulated B fields such that 68.27% (1σ) of vectors are within this relative-angle range. The relative angles found under this criterion represent the uncertainty of the VGT under the 1σ confidence interval. We then plot the results for each model and tracer in Figures 5 and 6.

Figure 5 represents the response of the VGT for simulation with self-gravity data. The blue circle represents ¹²CO, the orange square represents ¹³CO, and the green triangle represents C¹⁸O. The dashed horizontal line represents the random distribution. The upper panels represent the IGs, and the lower panels represent the VCGs. Figure 6 represents the result of simulations without self-gravity.

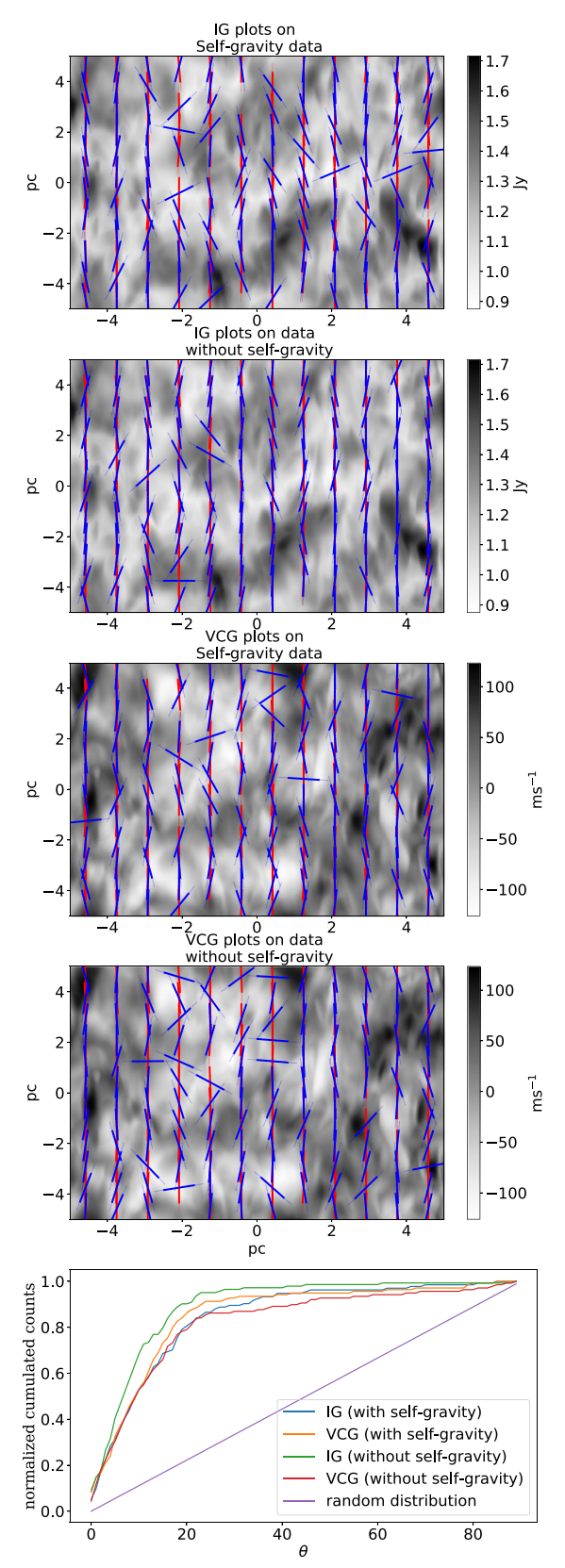


Figure 1. 12 CO b12 ($M_S = 0.92$, $M_A = 0.09$) data set. For each method (IG and VCG) and data set (with or without self-gravity), we plot the 2D vector plots and statistical results. The blue vectors represent the projected B fields from the simulation, and the red vectors represent the VGT-predicted B-field direction. The gray background represents moment 0 or 1 of the data cube. The relative angle between the simulated B field and the VGT-predicted direction is shown in the normalized cumulative plots.

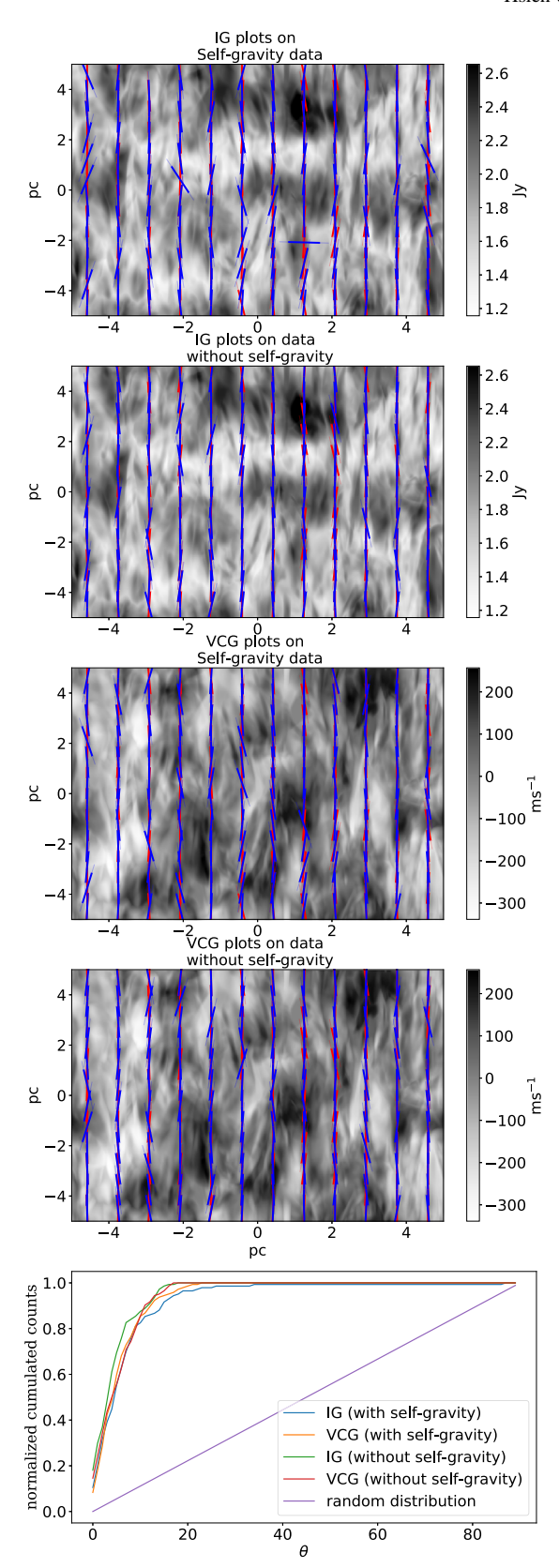


Figure 2. 12 CO b13 ($M_S = 1.95$, $M_A = 0.18$) data set. For each method (IG and VCG) and data set (with or without self-gravity), we plot the 2D vector plots and statistical results. The blue vectors represent the projected B fields from the simulation, and the red vectors represent the VGT-predicted B-field direction. The gray background represents moment 0 or 1 of the data cube. The relative angle between the simulated B field and the VGT-predicted direction is shown in the normalized cumulative plots.

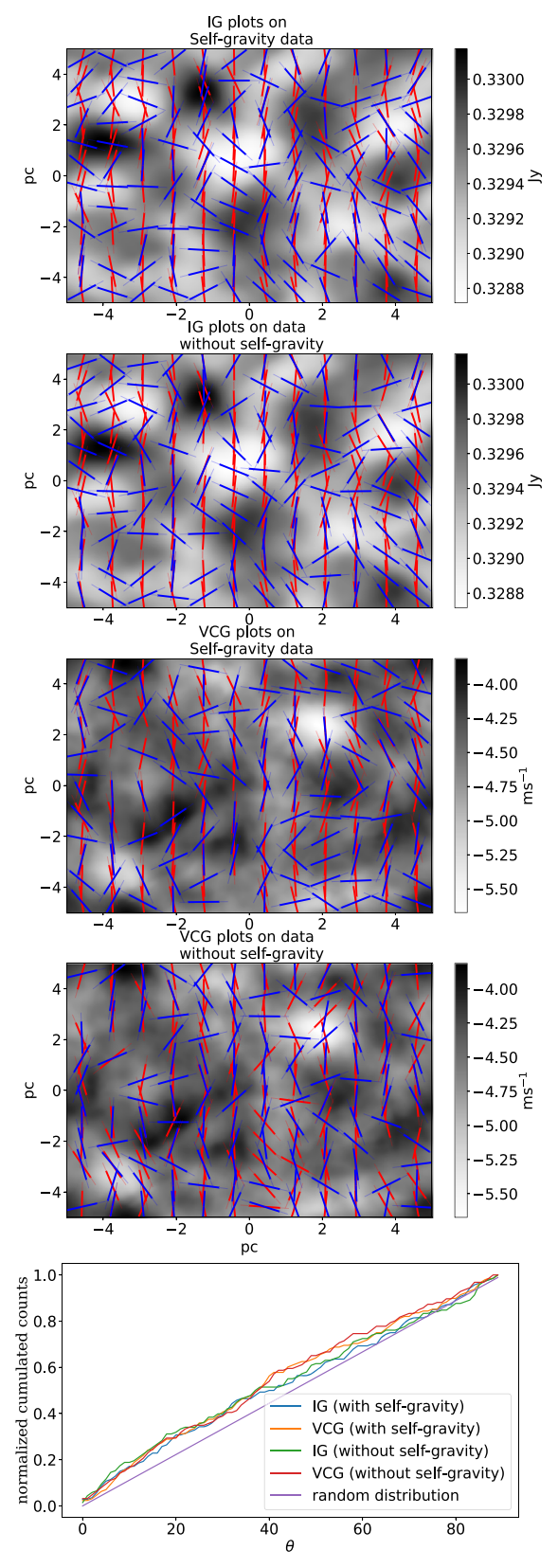


Figure 3. 12 CO b51 ($M_S = 0.05$, $M_A = 0.52$) data set. For each method (IG and VCG) and data set (with or without self-gravity), we plot the 2D vector plots and statistical results. The blue vectors represent the projected B fields from the simulation, and the red vectors represent the VGT-predicted B-field direction. The gray background represents moment 0 or 1 of the data cube. The relative angle between the simulated B field and the VGT-predicted direction is shown in the normalized cumulative plots.

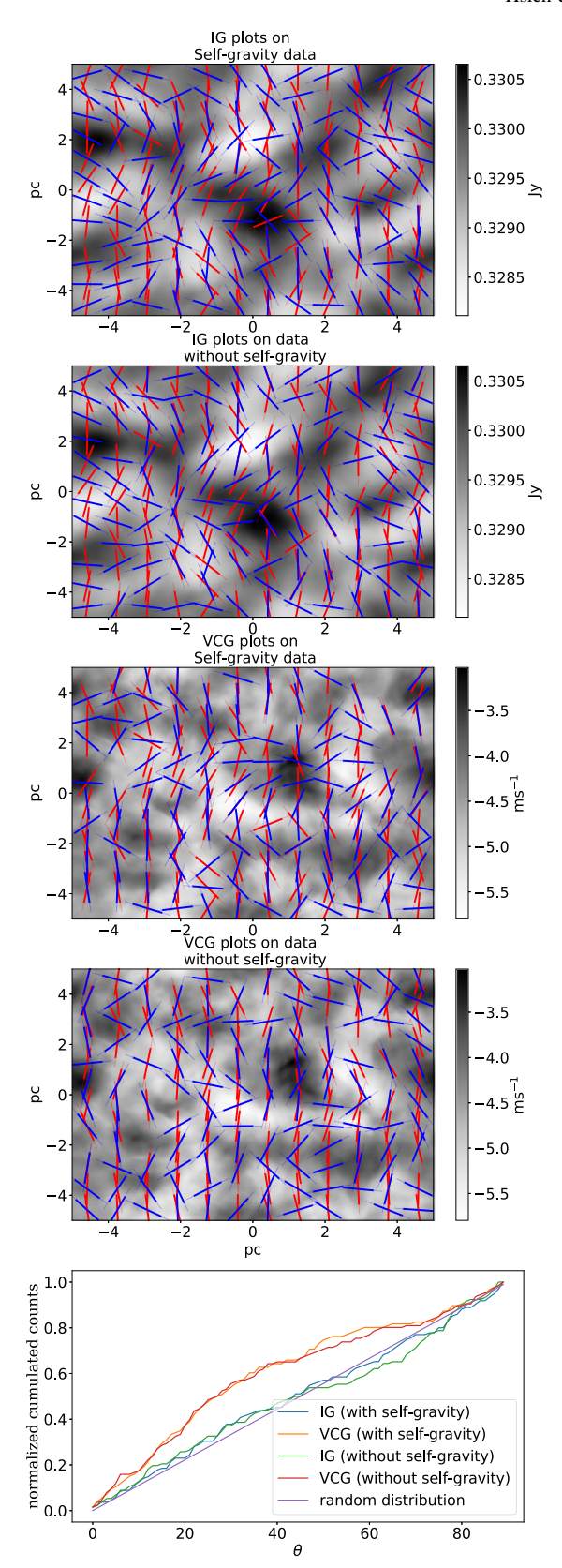


Figure 4. 12 CO b52 ($M_S = 0.10$, $M_A = 1.08$) data set. For each method (IG and VCG) and data set (with or without self-gravity), we plot the 2D vector plots and statistical results. The blue vectors represent the projected B fields from the simulation, and the red vectors represent the VGT-predicted B-field direction. The gray background represents moment 0 or 1 of the data cube. The relative angle between the simulated B field and the VGT-predicted direction is shown in the normalized cumulative plots.

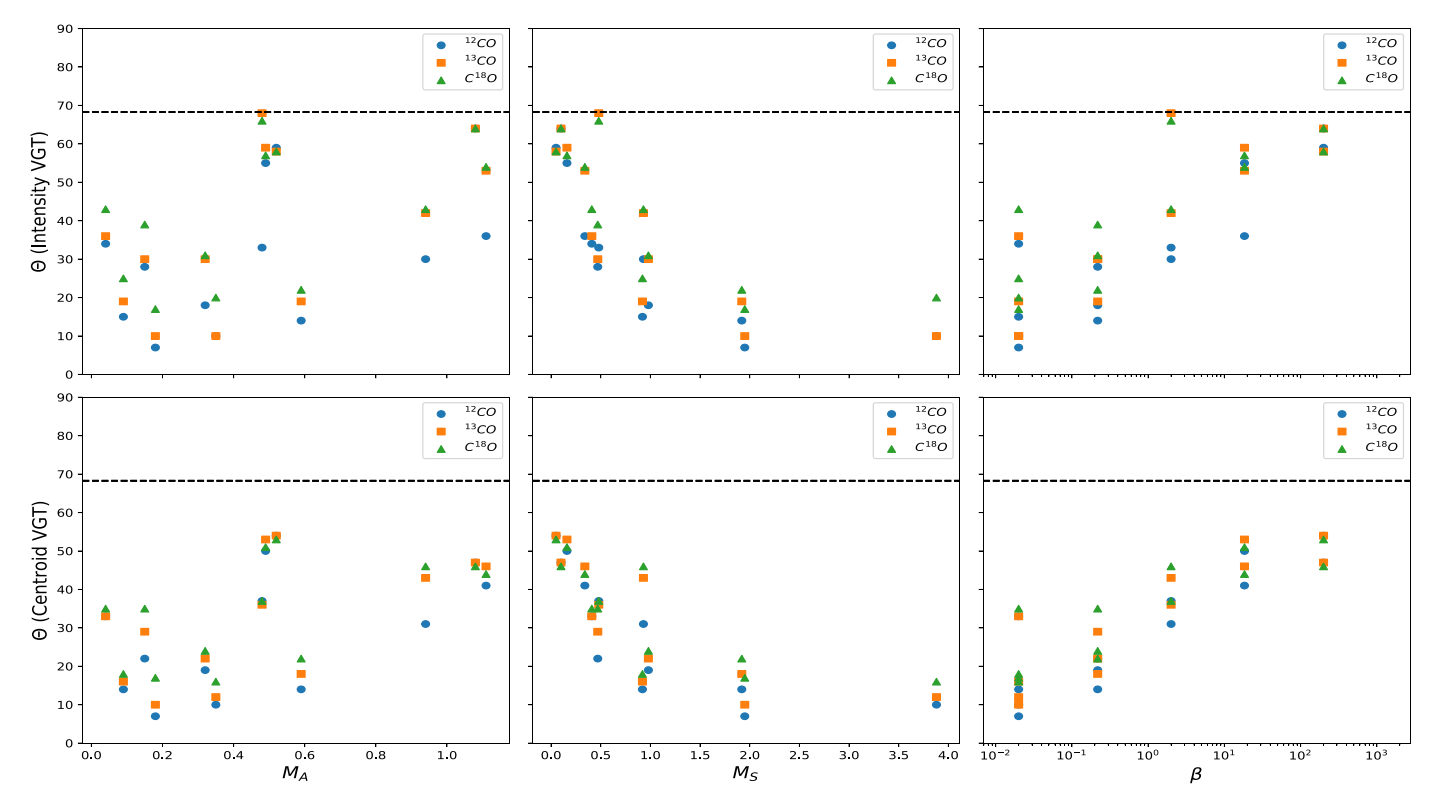


Figure 5. Plot of relative angle (between rotated gradients and magnetic field) such that the accuracy of IGs (top row) and VCGs (bottom row) is under 1σ uncertainty with respect to the variation of Alfvén Mach number $(M_A;$ left column), sonic Mach number $(M_S;$ middle column), and compressibility $(\beta = 2(M_A)^2/(M_S)^2;$ right column). Random distribution is marked as a horizontal dashed line. Turbulent MHD simulation data with self-gravity are used.

Comparing Figures 5 and 6, we find that the gradient vectors in the case of self-gravity are less aligned to the magnetic field direction compared to the case without self-gravity. Quantitatively, most of the differences between the two cases are within 4°.

The difference between with and without self-gravity is negligible. This indicates that in the diffuse region, the VGT can still be applied very well in the self-gravitating molecular clouds. The densities tested from all 14 models have ranges between 0.003 and 50 M_{\odot} pc⁻³, and the corresponding hydrogen number density is 0.004–70 cm⁻³. To put this into observational perspective, the GMCs have a density $n(H_2)$ (cm⁻³) of 100, molecular clouds have a density of 300, molecular clumps have a density of around 10³, and cloud cores have a density of 10⁵ (Bodenheimer 2011). Thus, the tested simulation cubes can be applied to GMCs that have similar number densities.

4.2. Response of Different Tracers

In Figures 5 and 6, we plot the relative angle of each model such that the accuracy of the VGT is under the 1σ uncertainty with respect to the variation of Alfvén Mach number (M_A) , sonic Mach number (M_S) , and compressibility $\beta = 2(M_A)^2/(M_S)^2$. In the cases of β and M_S , respectively, we can find a strong linear correlation between β or M_S and accuracy. With either the increasing of M_S or the decreasing of β , the VGT gives more accurate results. As for M_A , the overall plot is more scattered, so the correlation is not clear. Since β is proportional to M_A but inversely proportional to M_S , the increasing of M_S leads to a smaller β . Hence, M_S is the dominating factor that leads to a more accurate tracing. In the middle panels of Figures 5 and 6, as

the M_S increases to 2, the VGT predictions become better (smaller uncertainty). However, further increases of M_S after 2 will slightly increase the uncertainty. This is the same for both IGs and VCGs in with or without self-gravity conditions.

In the right panels of Figures 5 and 6, a large scattering is observed when the β value is small ($\sim 10^{-2}$). As for the M_A responses, the overall correlation is weaker than β and M_S . Before $M_A=0.2$, the VGT predictions, in general, have higher accuracy as M_A increases. After $M_A=0.2$, the accuracy of the VGT drops as M_A increases further. In both plots, there are concave down relationships with minimum points (at $M_A=0.2$ and $M_S=2$). However, there is a sharp increase in uncertainty for $M_A=0.5$, but for the M_S plots, there is no obvious feature similar to M_A .

For observational purposes, we set a criterion such that under the 1σ (68.27%) confidence interval, the VGT predictions are within a 20° angle deviation from the true simulated magnetic field. Above this criterion, the VGT can give very accurate magnetic field predictions. Under this criterion, in Table 1, we found that for ¹²CO and ¹³CO, the IGs are very accurate when $0.1 < M_A < 0.7$ (best when $M_A = 0.18$), $0.9 < M_S < 7.1$ (best when $M_S = 2$), and $0.02 < \beta < 0.2$. As for C¹⁸O, the IGs are very accurate when $0.2 < M_A < 0.4$ (best when $M_A = 0.18$), $0.02 < \beta < 0.2$. For C¹⁸O, the sonic Mach number range M_S for accurate IG predictions is smaller than the others. This result is consistent with Table 1 and Figures 5 and 6, which show that C¹⁸O has a larger uncertainty compared to the other two tracers. As for the VCGs, the accurate tracing ranges of M_S and M_A are the same as for the IGs for ¹²CO and C¹⁸O. However, for ¹³CO, the ranges are $0.9 < M_S < 3.9$ and

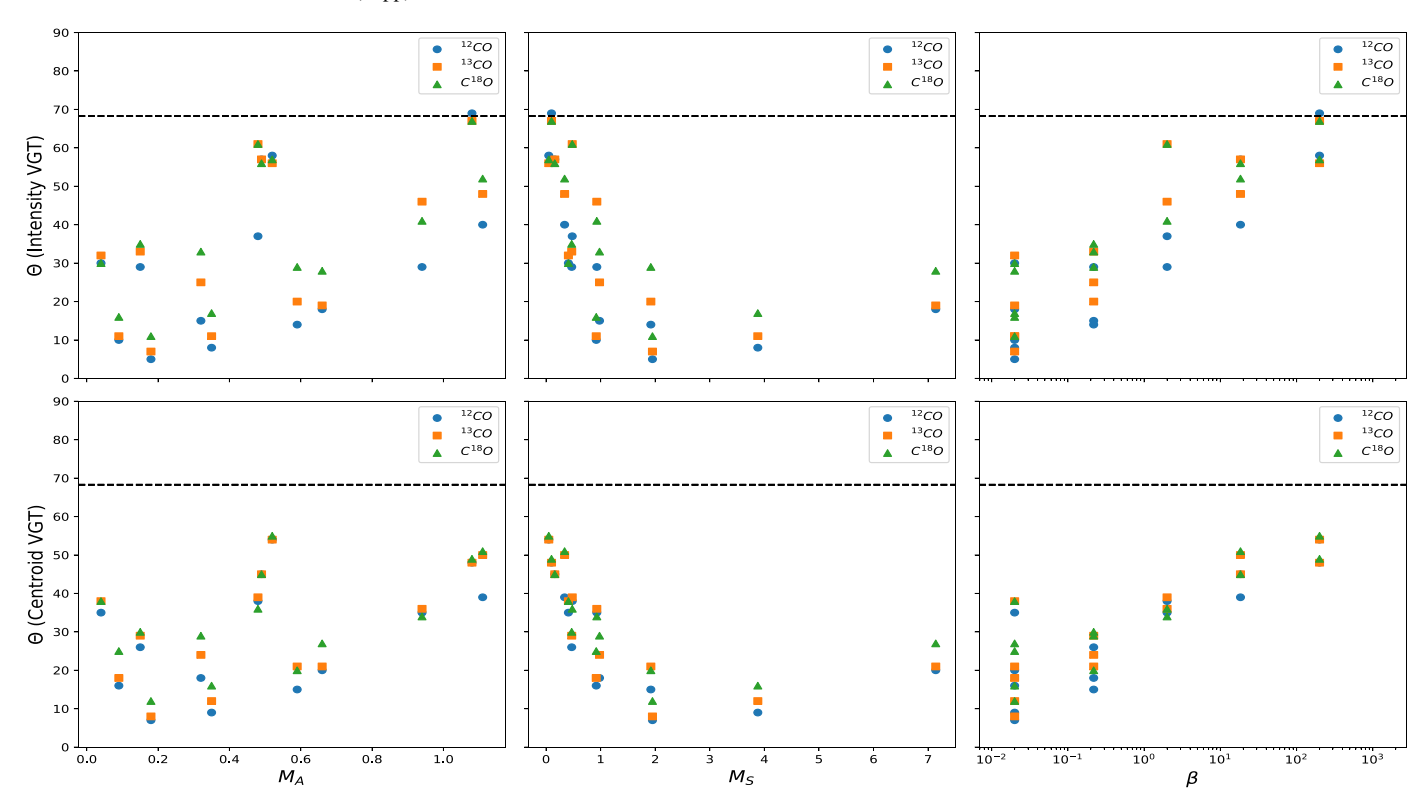


Figure 6. Plot of relative angle (between rotated gradients and magnetic field) such that the accuracy of IGs (top row) and VCGs (bottom row) is under 1σ uncertainty with respect to the variation of Alfvén Mach number $(M_A;$ left column), sonic Mach number $(M_S;$ middle column), and compressibility $(\beta = 2(M_A)^2/(M_S)^2;$ right column). Random distribution is marked as a horizontal dashed line. Turbulent MHD simulation data without self-gravity are used.

 $0.1 < M_{\rm A} < 0.4$, which are smaller than those for $^{12}{\rm CO}$ and $C^{18}{\rm O}$. The results are organized in Table 2.

4.3. VCGs versus IGs

In the previous sections, we studied how the VGT changes with respect to Alfvén Mach number M_A , sonic Mach number M_S , and β in the case of optically thick and thin media. In this section, we will inspect how the change of moment maps will alter the prediction of the magnetic field using the VGT. Figures 5 and 6 show the mean relative-angle deviation between the magnetic field predictions from both the VGT and emulated dust polarizations for both self-gravitating and non-self-gravitating simulations, respectively. The results from the IGs are shown in the top row of Figures 5 and 6, while those for centroid gradients are shown in the bottom row.

In general, the centroid gradients have slightly better performance when compared to the IGs. For the 13 CO case, IGs and VCGs have very similar results. For model b23 ($M_S = 1.92$, $M_A = 0.59$), the VCGs have a relative angle of 21°, while the IGs give an uncertainty of 20° for the self-gravity data set. Under the 20° criterion, this resulted in the difference of range shown in Table 2.

The VCGs of C¹⁸O show a slightly better performance than the IGs of ¹³CO and ¹²CO. The crucial reason behind this is that the velocity channels in the wing side of the spectral line are more velocity-like and diffuse (Lazarian & Pogosyan 2000) when the channel width is optically thin. Since the wing side has more weighting compared to the central part of the spectral line in the process of computing the velocity centroid, the velocity centroid displays more velocity eddy information compared to the total intensity map. As a result, the VCGs are more accurate, since velocity eddies are direct probes of

turbulence data, while density eddies are indirect consequences of fluid compression (Cho & Lazarian 2003).

In the diffuse region, it is expected that gravity takes a negligible role in regulating the gas motions in molecular clouds. As a result, the gas motions are channeled by the local magnetic field directions, and therefore the assumption for the VGT holds for diffuse media (see Section 2). However, it is discussed in both Yuen & Lazarian (2017b) and Lazarian & Yuen (2018b) that the gradient orientation changes from \bot B to $\parallel B$ according to the stage of collapse (aka rerotation). However, for the two sets of figures we show in Figures 5 and 6, we spot negligible differences in terms of the mean angle deviations. Therefore, we conclude that the effect of gravity in the self-gravity simulations used in Figure 5 is not strong enough to trigger the rerotation of gradients.

4.4. Saturation After Radiative Transfer and the Possibility of 3D Magnetic Field Mapping through Different Tracers

We plot the velocity spectral profile for three different tracers in Figure 7. After carrying out the radiative transfer calculation, we observed many interesting features. First of all, the intensity of ¹²CO is much higher than that of ¹³CO and C¹⁸O. This is expected in observations, as the abundance of CO isotopes is much lower than that of ¹²CO.

While the optical depth of ¹²CO is significantly higher than that of ¹³CO, it is possible for the gradients of the ¹³CO tracer maps to perform better than that of ¹²CO in probing the direction of the magnetic field around the self-gravitating core. This is because, around the center of gravity of an observed molecular cloud, the number of pixels that are truthfully sampled by ¹³CO is much higher than that of ¹²CO. Since the accuracy of the gradients relies on the structures displayed by

Table 2
The Range of M_A and M_S Such That Under 1σ Uncertainty, the Relative Angle between the VGT and True Simulated B Fields is Less Than 20°

Method		IGs		VCGs			
	¹² CO	¹³ CO	C18O	¹² CO	¹³ CO	C18O	
$M_{\rm A}$	[0.1, 0.7]	[0.1, 0.7]	[0.2, 0.4]	[0.1, 0.7]	[0.1, 0.4]	[0.2, 0.4]	
M_S	[0.9, 7.1]	[0.9, 7.1]	[2.0, 3.9]	[0.9, 7.1]	[0.9, 3.9]	[2.0, 3.9]	

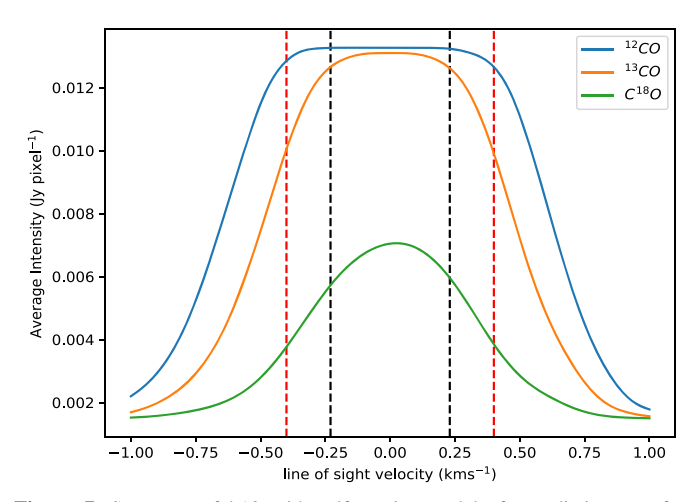


Figure 7. Spectrum of b13 with self-gravity model after radiative transfer calculation. The blue line represents ¹²CO, the orange line represents ¹³CO, and the green line represents C¹⁸O. The black and red dashed lines mark the region that is optically thick and in which the intensity is saturated for ¹³CO and ¹²CO, respectively.

neighboring pixel values, it is natural for the gradients of ¹³CO maps to perform better in tracing magnetic fields than those of ¹²CO due to the differences in sampling size.

However, in the synthetic image cubes, the molecular intensity will be saturated in the line core, where the relative velocity is small. This can be understood by the fact that when the medium is optically thick, we cannot see through it, and what we will observe will be the gases on the surface. In Figure 7, we use the black dashed lines to roughly mark out the region that is optically thick. For 12 CO, the medium is optically thick when $v \in [-0.4 \sim 0.4 \, \mathrm{km \, s^{-1}}]$. As for 13 CO, the opaque region is between -0.23 and 0.23 km s⁻¹, and there is no saturation in C¹⁸O in our sample synthetic data in Figure 7. The situation mentioned above changes in terms of synthetic maps, as those improperly sampled pixels are now displayed as a constant (see Figure 7). Those saturated pixels, while not related to the kinematic properties of molecular gas, form anisotropic structures. As a result, the appearance of these constant pixels does not decrease the tracing power for optically thick tracers, and the alignment measure of optically thick tracers should be higher than that of optically thin tracers unless the density structures are strongly distorted by gravity.

In the case of saturation, the contribution of those saturated channels (e.g., velocity channels with $v \in [-0.4 \text{ to } 0.4 \text{ km s}^{-1}]$ in the case of ¹²CO) will be zero when performing gradients, since they are just intensity maps having constant pixel values. As a result, when computing the gradients of integrated intensity or velocity centroid maps, only the velocity channels outside the saturated regions will contribute. In theory, by using different tracers, we can trace magnetic fields in regions corresponding to different line-of-sight velocities. However, the gradients of the material distribution in the velocity space

are very difficult to utilize in building up the 3D structure of the magnetic field, since the effect of velocity caustics is taking effect (Lazarian & Pogosyan 2000). It would be convenient to make use of the fact that, when the molecular cloud is optically thick for a certain tracer, only the contribution with a line-of-sight deepness $z < \tau$ will be positively contributing when using the VGT. As as result, the VGT can only trace the B field associated with the surrounding gases in the molecular clouds. Therefore, line-of-sight distance-dependent magnetic field tomography can be achieved by stacking the VGT results from different molecular tracers.

5. Discussion

5.1. Strengths and Limitations of the VGT in the Self-absorbing Media

The VGT shows a nice adaptivity in numerous physical conditions, which provides a robust way to get magnetic field orientations with high accuracy. From our study, the VGT even performs excellently in the case of self-gravitating and self-absorbing media. However, understanding the limitations of the VGT to work in self-absorbing media is crucial for the community to utilize and further develop the VGT with molecular tracer maps.

As we know, polarization data are among the most reliable ways to obtain the magnetic field orientation. However, they are only universally available with some state-of-the-art interferometric instruments, which require prior knowledge of the dust grain alignments and usually also an understanding of background emission and the cost of obtaining such measurement on the ground or even in space. Fortunately, the VGT makes use of readily available spectroscopic data, such as the CHIPASS synchrotron survey, HI4PI neutral hydrogen atom distribution survey, and COMPLETE survey, to provide nearly equally accurate measurements of the magnetic field orientations, which can also be cross-checked by using different tracers on the same piece of observation data. Previous series of papers (Yuen & Lazarian 2017a; Lazarian & Yuen 2018b; Yuen et al. 2018) already showed that the VGT can provide comparable or even better field-tracing abilities in both numerical and diffuse observational data. There is no doubt that the VGT can be synergistically used with dust/synchrotron polarization data in determining the morphology of the projected magnetic field (Lazarian et al. 2017; Lazarian & Yuen 2018a).

While the VGT is very powerful in predicting the magnetic field morphology using just spectroscopic data, there are some limitations for the method that must be considered. The first and most important issue for the VGT is that it is based on anisotropic properties of turbulent MHD, so it can only be used for turbulent systems. From this work, we found that it works best for supersonic turbulence systems with $0.02 \le \beta \le 0.2$. For molecular clouds with density $n(H_2) \sim 100 \, \text{cm}^{-3}$, the typical magnetic field strength is on the order of $\sim 10 \, \mu\text{G}$ (Crutcher et al. 2010). With a typical gas temperature of $\sim 10 \, \text{K}$

(Wilson et al. 1997), the turbulence sound speed is on the order of \sim 0.2 km s⁻¹. From these observational constrains, it can be shown that the criteria $0.02 \leqslant \beta \leqslant 0.2$ are commonly satisfied in GMCs.

For the observational implementations of the VGT, it is crucial to note that the VGT is based on group statistics; i.e., the technique depends highly on the quality of the data, and it can degrade the spatial resolution of the B field predicted for at least 20 times (Lazarian & Yuen 2018a). A block-average technique with Gaussian fitting of gradient angles ensures the accuracy of VGT predictions on magnetic fields. A block size of 20 used in the VGT requires 20² of independent measurements, which corresponds to an area of 20² beam size in the observational term. The final inferred magnetic field direction represents the average magnetic field direction within the block. Thus, the observational map size–to–beam size ratio constrains the number of magnetic field vectors that can be predicted by the VGT. As for the selection of block size, it is determined by how many independent measurements (beam size) are needed in order for the gradient angle to reach a Gaussian-like distribution. Observers applying the VGT should include enough independent measurements to ensure the shifted Gaussian distribution for block averaging. This is a necessary condition for applying the VGT to observational data. In addition, if the observation is very noise-dependent (has strong correlated noise), the gradient technique cannot extract the magnetic field orientation, even with the use of a very large block size. Fortunately, the shape of the gradientangle distribution will tell whether the statistics of gradients are qualified for deriving a meaningful prediction of magnetic field in the region of interest.

The VGT also faces limitations when dealing with optically thick molecular tracer maps, since it is technically an edgedetection algorithm relying on the turbulence statistics theory (Goldreich & Sridhar 1995; Lazarian & Vishniac 1999) in predicting the direction of the magnetic field. If the pixels in the molecular tracer map are saturated in the central part of the velocity channels, such as in the case of ¹²CO, then the ability to use gradients in these velocity channels will be significantly limited. The detailed theoretical and numerical study of saturation effects will be addressed in a future paper (C.-h. Hsieh et. al 2019, in preparation). Comparatively, the polarization fraction in the case of optically thick clouds is usually low (Fissel et al. 2010, 2016), since these clouds with low optical depth are usually self-gravitating. The prediction from polarization might not be helpful in determining the direction of the magnetic field without referring to other independent measures.

Gravitational collapse is one of the main forces affecting the performance of the VGT in tracing the magnetic field in molecular clouds. In collapsing regions, the gradient field becomes distorted, and the direction of the gradients no longer aligns perpendicularly to the magnetic field; it is parallel. To account for this, the compensatory rerotation of gradients (i.e., rotating the gradient by 90° again) should be applied to the gradient (Hu et al. 2018b). In this study, we stop the simulation before reaching the Truelove criterion, which ensures that the isothermal self-gravitating medium is not collapsing.

Foreground absorption or background emission have little effect in limiting the predicting power of the VGT. Even though foreground absorption can cause significant changes in the intensity structure of the observed source, distorting the

vectors predicted by the VGT, such effects can be easily avoided by separating the source out in velocity space. Unlike dust polarization data, which are integrated in the broad frequency domain, the VGT can be applied to moment 0 or 1 maps calculated from the channels that only contain the source. By doing the channel selection, VGT has a degree of freedom to separate out the source in the line of sight in velocity space.

There are also some important issues when applying the VGT to radio interferometric data, and some preprocessing is needed. The first is that the angular resolution of interferometric observations will be slightly distorted due to the noncircular beam effect. Using an elliptical beam to sample the source would cause the data to have position-angledependent angular resolution. The direction along the major axis of the elliptical beam would have lower angular resolution, causing the structure to be slightly elongated in the direction of the major axis of the elliptical beam. This would cause a systematic error when the VGT is applied. In order to obtain unbiased sampling data before applying the VGT, it is advised that observers convolve the beam into a circular beam before applying the VGT to eliminate this systematic error. Also, proper handling of noise in real observational data is required. Observers should perform a careful job to remove all of the radio artifacts due to sidelobes; any leftover sidelobe will cause a systematic error in the VGT. If the deconvolution is done correctly, the noise in the radio data should be random Poisson noise. Random white noise does not produce a systematic error in the VGT; however, it adds to the flat background when fitting a shifted Gaussian in the block-averaging phase. As a criterion, if the constant area is larger than the Gaussian area fitted, then the VGT prediction in that block is discarded. Additional smoothing can be used to average out this random noise; however, the spatial resolution of the VGT would decrease. Observers should choose a smoothing scale to have the right balance between spatial resolution and accuracy in the Gaussian fitting in block averaging.

5.2. Possible Effects of Driven and Decaying Turbulence Simulation on the Performance of the VGT

Supersonic turbulence played an important role in regulating the dynamics of molecular clouds and star formation (Larson 1981). Currently, there are two ways to simulate turbulence in molecular clouds, and each is closely tied to a different view on cloud dynamics. Decaying turbulence simulation initiates a turbulence field and allows it to decay. Without further injection of energy, the turbulence will decay with a characteristic timescale of roughly 1 crossing time (Mac Low & Klessen 2004). After losing the turbulence support, the molecular cloud would undergo global collapse and trigger star formation. To obtain the observed low star formation rate, in this picture, the molecular cloud must be a short-lived transient structure (Elmegreen 2000). Driven turbulence simulations, on the other hand, allow longer-lived molecular clouds, and the turbulence energy is constantly injected into the system. Such a driven turbulent system has been observed in the L1555 lowmass star-forming region (Swift & Welch 2008).

In this study, driven turbulent simulations are used to study the behavior of the VGT. The VGT is expected to perform better in driven turbulent simulations compared to decaying turbulent simulations. This is because, after losing turbulent pressure support, the density fields of decaying turbulent simulations are expected to be more clustered around the collapse center. When the turbulent driving mechanism is turned off, the density profile is expected to evolve closer to a freefall profile, $\rho \propto r^{-1.5}$ (Offner et al. 2008). A stronger gravitational effect is expected in the decaying turbulent simulations, resulting in the more pronounced distortion of the VGT-predicted vectors. Denser tracers such as 13 CO and 18 O are expected to be strongly affected.

Driven turbulence simulations, on the other hand, introduce an unphysical driving force, which will result in a large artificial mass flux between low-density regions and highdensity regions. A high mass flux implies that more materials are affected by turbulent eddies and hence increase the performance of the VGT. Driven turbulence simulations are expected to have a steeper velocity profile, $\sigma \propto r^{0.5}$, compared to decaying turbulence simulations (Jijina et al. 1999; Offner et al. 2008). The steeper slope in the velocity profile ensures that the magnitude of the gradient is large enough to perform the VCG. The increase in mass flux also resulted in a flatter density profile, $M(R) \propto R$, in the driven turbulent simulation (Offner et al. 2008). An increase in mass flux artificially increases the intensity in the diffuse region. Since moment 1 is the intensity-weighted average velocity and moment 0 is an intensity map, this would result in the magnetic field traced along the line of sight being slightly biased toward the diffuse region, hence improving the performance of ¹²CO, a lowdensity tracer, in both the IG and VCG methods.

In both driving and decaying turbulence simulations, ¹²CO is expected to perform better than ¹³CO and C¹⁸O. In the driving turbulence case, ¹²CO is enhanced by the increase in mass flux in the diffuse regions. In the decaying turbulence simulation case, dense tracers such as ¹³CO and C¹⁸O are more strongly affected by the stronger collapsing motion.

5.3. Extracting 3D Magnetic Field Structure by Utilizing Multiple Molecular Tracer Data

Molecular tracer maps with different optical depths provide spectroscopic information about gas dynamics up to a certain line-of-sight depth. As shown in Figure 7, some tracers are optically thick in some velocity channels. In these fully saturated channels, the magnetic field information is not traced. This motivates us to investigate an important question: whether or not we can use the VGT to trace different layers of magnetic fields in the line of sight by utilizing multiple molecular tracer data.

The concept of "gradient tomography" was first discussed in Lazarian & Yuen (2018a) by considering the effective accumulation of the line-of-sight deepness of synchrotron polarization data with a different wavelength. Both the synchrotron polarization data with the presence of strong Faraday rotation effects and the gas spectroscopic data with the presence of optically thick radiative transfer effects share the same concept that the contribution of gas dynamics with a lineof-sight deepness larger than some certain physical boundary would be effectively noise. Lazarian & Yuen (2018a) showed that, by stacking the gradient maps from the polarized synchrotron intensities measured from different frequencies, one can create the 3D tomography information of the magnetic field. The number of layers in the gradient tomography completely depends on how many individual frequency measurements one has taken for the synchrotron data. The analogous idea can actually be implemented in the case of multiple molecular tracer maps but in a much coarser content.

For example, it is theoretically possible to stack the gradient maps from ¹²CO, ¹³CO, and C¹⁸O to create a three-layer tomography map, which is shown observationally in Y. Hu et al. 2018, in preparation.

One might also question whether the 3D magnetic field is measurable if stacking multiple dust polarization emissions in different wavelengths similar to Lazarian & Yuen (2018a). However, dust polarimetry faces several limitations in tracing the magnetic field. Not only does the dust grain fail to align at a high optical depth if there are no illuminating sources inside the cloud (Lazarian 2007), but the far-infrared polarization also suffers from the confusion effect when the cloud is in the galactic plane. It is therefore not practical to stack multiple dust emission maps with different wavelengths in acquiring the 3D magnetic fields similar to the 3D synchrotron polarization gradients (Lazarian & Yuen 2018b) or the Faraday tomography method (Burn 1966).

In any case, the 3D studies of absorbing species are complementary to the studies in H I and synchrotron polarization. This gives the 3D structure of the magnetic field in the galactic magnetic ecosystem.

5.4. Synergy with the Latest Development of the VGT

5.4.1. Improving the Accuracy of B-field Orientation Tracing by Principal Component Analysis VGT

In terms of tracing the magnetic field in the ISM, accuracy is the most important aspect. Hu et al. (2018a) demonstrated that the accuracy of the VGT can be significantly improved by principal component analysis (PCA), which is widely used in image processing. In this work, the VGT also shows a robust performance in tracing the magnetic field with the presence of molecular media. Furthermore, we expect that PCA can also extract the spectroscopic information that is most valuable for the VGT, considering that the emission from molecular media and then the synergy of the VGT and PCA would further improve the accuracy.

5.4.2. Acquisition of M_s, M_A

The magnetization of the ISM is also one crucial aspect of the star formation theory. Recently, the VGT has been introduced in Lazarian et al. (2018) to obtain a reliable estimation of the magnetization of the media in H I data. In this work, we show that different molecular tracers contain individual information due to their own optical depth. Hence, we see the possibility of constructing the 3D strength map of the magnetic field by combining different molecular tracers.

5.4.3. The Relationship between Effective Optical Depth τ and Channel Optical Depth and Its Implications for the VGT

In Figure 7, we plot the average intensity in each velocity channel, and this spectrum offers great insight as to how IGs operate. It tells us the contribution of the magnetic fields at each channel traced by the IG method. It also explains why ¹²CO performs better than ¹³CO and C¹⁸O.

To illustrate the concept, we first demonstrate the relationship between effective optical depth $\tau_{\rm eff}$ for the moment 0 map and optical depth in individual velocity channels. Consider the simple two-channel PPV cube shown in Figure 8. In the PPV cube, the temperature is set at a uniform 10 K. When we add the two channels to calculate the moment 0 map, the effective

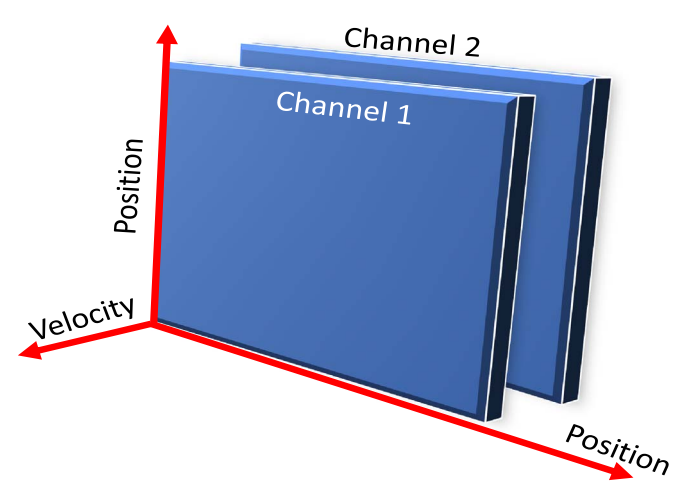


Figure 8. Cartoon diagram of a two-channel PPV cube.

optical depth added is as follows:

$$\frac{I_{1} + I_{2}}{2} = I_{bg}e^{-\tau_{\nu}} + \frac{I_{10 \text{ K}}[1 - e^{-\tau_{1}}] + I_{10 \text{ K}}[1 - e^{-\tau_{2}}]}{2},$$

$$I_{avg} = I_{bg}e^{-\tau_{\nu}} + I_{10 \text{ K}} - \frac{I_{10 \text{ K}}[e^{-\tau_{1}} + e^{-\tau_{2}}]}{2},$$

$$e^{-\tau_{avg}} = \frac{[e^{-\tau_{1}} + e^{-\tau_{2}}]}{2}.$$
(4)

Channel 1 is much more optically thick than channel 2 $(\tau_1\gg\tau_2),\ e^{-\tau_{avg}}\approx \frac{e^{-\tau_2}}{2},$ or roughly $\tau_{avg}\approx\tau_2$. This simple example illustrates an import implication for IGs: optically thick channels contributed less in the effective optical depth calculations. In the IG method, most of the magnetic fields traced are in the tail distribution of Figure 7. In the central saturated region, few or no magnetic fields are traced, and this resulted ^{12}CO , a high velocity diffuse region tracer, to have better IG performance. A more in-depth discussion of saturation and which region of the magnetic field is traced will be addressed in a future paper (C.-h. Hsieh et. al 2019, in preparation).

5.4.4. Locating the Self-gravitating Regions

Furthermore, since the VGT is available even with the presence of self-gravity, it is possible to understand how magnetic fields behave inside the GMCs in the stage of collapsing and help us to shape the star formation theory into a better form. On the other hand, the spectroscopic data are obtained by using molecular tracers, such as ¹²CO, ¹³CO, C¹⁸O, and so on, which contain individual information from low-density regions to high-density regions. By using the VGT, it is possible to extract the magnetic field morphology in different regions or layers and then construct the 3D magnetic field morphology with multiple stages. One obstacle is that the velocity field would be distorted in a collapsing region. Hence, in collapsing regions, we usually need to apply compensation for the distortion to the VGT for accurate tracing.

5.5. Comparison with Earlier Works

The VGT was initially introduced and studied without taking into account the effects of self-absorption of radiation (Yuen & Lazarian 2017a, 2017b). Such studies are most relevant to diffuse H I and other media with low absorption. For molecular

gas tracers such as CO used in this paper, radiative transfer is crucial in order to get the correct result for the VGT. González-Casanova et al. (2017) estimated the ability of VCGs in tracing the magnetic field with the presence of absorbing media for the case of 13 CO J=2-1 emission. They also demonstrated that the VGT is able to trace the magnetic field in media with different CO abundances, densities, and optical depths. However, the change of CO abundances and densities might introduce non-LTE and saturation effects. In this work, we extended González-Casanova et al.'s (2017) study with typical CO abundances inferred based on observation (Wilson 1999, 1999; Wilson et al. 2016). We study both the IGs and VCGs, and we also explore the effect from different molecules of 12 CO, 13 CO, and 18 O with emission line J=1-0.

The optical depths are different for different species. In terms of the applicability of multiple tracers in observations, we numerically demonstrate the possibility of obtaining 3D magnetic field morphology by combining different molecular tracers. Furthermore, we consider the effect of weak self-gravity and show that the VGT is still applicable. The effect of line-saturation effects in the VGT will be investigated in our future work.

The HRO is a statistical way to determine the relative orientation of the magnetic field and density gradients (Soler et al. 2013). To avoid confusion, one should distinguish that IG is the technique to trace magnetic fields in space, while HRO does not have this ability. An IG can even be used to study shocks and regions of gravitational collapse, etc. (Yuen & Lazarian 2017b; Lazarian & Yuen 2018b) but does not require any polarization data to get this information. On the contrary, the HRO compares the relative orientation of the density gradients and polarization directions as a function of column density. Since the HRO is only a tool to study the statistical correlation, we expect to get more information between the VCGs and the magnetic field by using the HRO.

6. Conclusion

In this work, we estimate the ability of the VGT to trace the magnetic field with the presence of a molecular medium (¹²CO, ¹³CO, and C¹⁸O), as well as with and without self-gravity cases. We demonstrate that the VGT shows robust performance in the presence of the radiation transfer and self-gravity. As a part of the VGT, we use IGs, which are a derivative approach based on applying the VGT procedures to emission intensities. We summarize as follows:

- 1. The VGT is most accurate in ¹²CO. For ¹³CO and C¹⁸O, the dispersion of the relative angle is larger, as shown in Table 1. This is because ¹²CO only traces optically thin channels that correspond to the diffuse region.
- 2. The centroid gradient method works better than the IG method. Velocity weights on high-velocity channels increase the weighting for the diffuse region.
- 3. As the sonic Mach number M_S increases, the magnetic field direction get more perpendicular to the IG. This effect is also present to a lesser extent for the centroid gradient.
- 4. For systems that have values within $0.02 < \beta < 0.2$ and $M_S \geqslant 1.0$, the VGT has an uncertainty of less than 20° under the 1σ (68.27%) confidence interval and can make very accurate B-field predictions.

5. For a density $n({\rm H_2})({\rm cm^{-3}})$ between 0.004 and 70 cm⁻³, applying the VGT to self-gravity data shows a slightly larger dispersion compared to the data without self-gravity.

C.H.H. and S.P.L. acknowledge support from the Ministry of Science and Technology of Taiwan with grant *MOST* 106-2119-M-007-021-MY3. A.L. acknowledges the support of the NSF AST 1816234 and NASA AAG1967 grants.

Appendix A SPARX

SPARX stands for "Simulation Package for Astronomical Radiative Transfer (Xfer)." As part of the Coordinated Hydrodynamic and Astrophysical Research, Modeling, and Synthesis (CHARMS) initiative, which focuses on bridging theory and numerical astrophysics with observational astrophysics at the Theoretical Institute for Advanced Research in Astrophysics in ASIAA, SPARX is a multipurpose radiative transfer calculation tool. It is designed to generate synthetic (non-)LTE atomic and/or molecular spectral and dust continuum images.

SPARX solves the specific intensity I_{ν} at a given frequency ν with the standard radiative transfer equation,

$$\frac{dI_{\nu}}{ds} = -\kappa_{\nu}I_{\nu} + \epsilon_{\nu},\tag{5}$$

where κ_{ν} is the absorption coefficient and ϵ_{ν} is the emission coefficient at the given frequency ν . The above equation can be rearranged into form

$$\frac{dI_{\nu}}{d\tau_{\nu}} = -I_{\nu} + S_{\nu},\tag{6}$$

where $d\tau_{\nu} \equiv \kappa_{\nu} ds$ is the optical depth, and $S_{\nu} \equiv \epsilon_{\nu}/\kappa_{\nu}$ is the source function. The intensity can be evaluated numerically by

$$I_{\nu} = \sum_{\forall c \text{ell}} S_{\nu} (1 - e^{-\Delta \tau}) e^{-\tau}.$$
 (7)

We note that κ_{ν} and ϵ_{ν} are related to the Einstein A and B coefficients and the gas density n,

$$\kappa_{ii}(\nu) = n_i A_{ii} \phi(\nu), \tag{8}$$

$$\epsilon_{ii}(\nu) = (n_i B_{ii} - n_i B_{ii}) \phi(\nu), \tag{9}$$

$$S_{ij} = \frac{n_i A_{ij}}{n_j B_{ji} - n_i B_{ij}},\tag{10}$$

where i and j denote the starting and ending energy states of the molecular transition under consideration, n_i is the gas density at energy state i, and $\phi(\nu)$ is the Doppler broadening function,

$$\phi(\nu) = \frac{c}{b\nu_0\sqrt{\pi}} \exp\left(\frac{-c^2(\nu - \nu_0)^2}{\nu_0^2\sigma^2}\right),\tag{11}$$

in which σ is the line width summed by the thermal speed and turbulent speed, and c is the speed of light.

The Einstein coefficients themselves in the above equations are related in the following manner:

$$\frac{g_j B_{ji}}{g_i B_{ij}} = 1, (12)$$

$$\frac{A_{ii}}{B_{ii}} = \frac{8\pi h \nu_0^3}{c^3},\tag{13}$$

where g_i is the statistical weight of the energy state i, and h is the Planck constant. In this work, we consider the rotational transitions of carbon monoxide that have a statistical weight of $g_J = 2J + 1$. Additional molecular data required for the calculation are retrieved from the LAMDA database (http://home.strw.leidenuniv.nl/moldata/).

The level populations n_i and n_j of energy states i and j required for evaluating κ_{ν} and ϵ_{ν} in the radiative transfer equations should be solved through detailed balancing. This, in turn, depends on the incoming radiation. Therefore, in the general non-LTE calculation, the specific intensity (I_{ν}) , mean radiation field (integral of I_{ν}), and level populations n_i are solved iteratively.

In this work, the molecular transitions under consideration should meet the LTE assumption. The molecular-level populations can therefore be described by the Boltzmann distribution,

$$\frac{n_j}{n_i} = \frac{g_j}{g_i} e^{-\frac{-h\nu_0}{kT}} \tag{14}$$

or

$$\frac{n_i}{N} = \frac{g_i e^{\frac{-E_i}{kT}}}{Z},\tag{15}$$

where N is the total molecular density and Z, the partition function, can be expressed as

$$Z = \sum_{i \in \text{ensemble}} g_i e^{\frac{-E_i}{kT}}.$$
 (16)

For further detailed description of the SPARX software and the benchmark problem (van Zadelhoff et al. 2002) the package has been tested against, we refer the reader to the software website (https://sparx.tiara.sinica.edu.tw/).

Appendix B ¹³CO Cumulative Plots

We plot the ¹³CO results for models b12, b13, b51, and b52 in Figure 9. ¹³CO shows similar results for the 4 models as compared with ¹²CO.

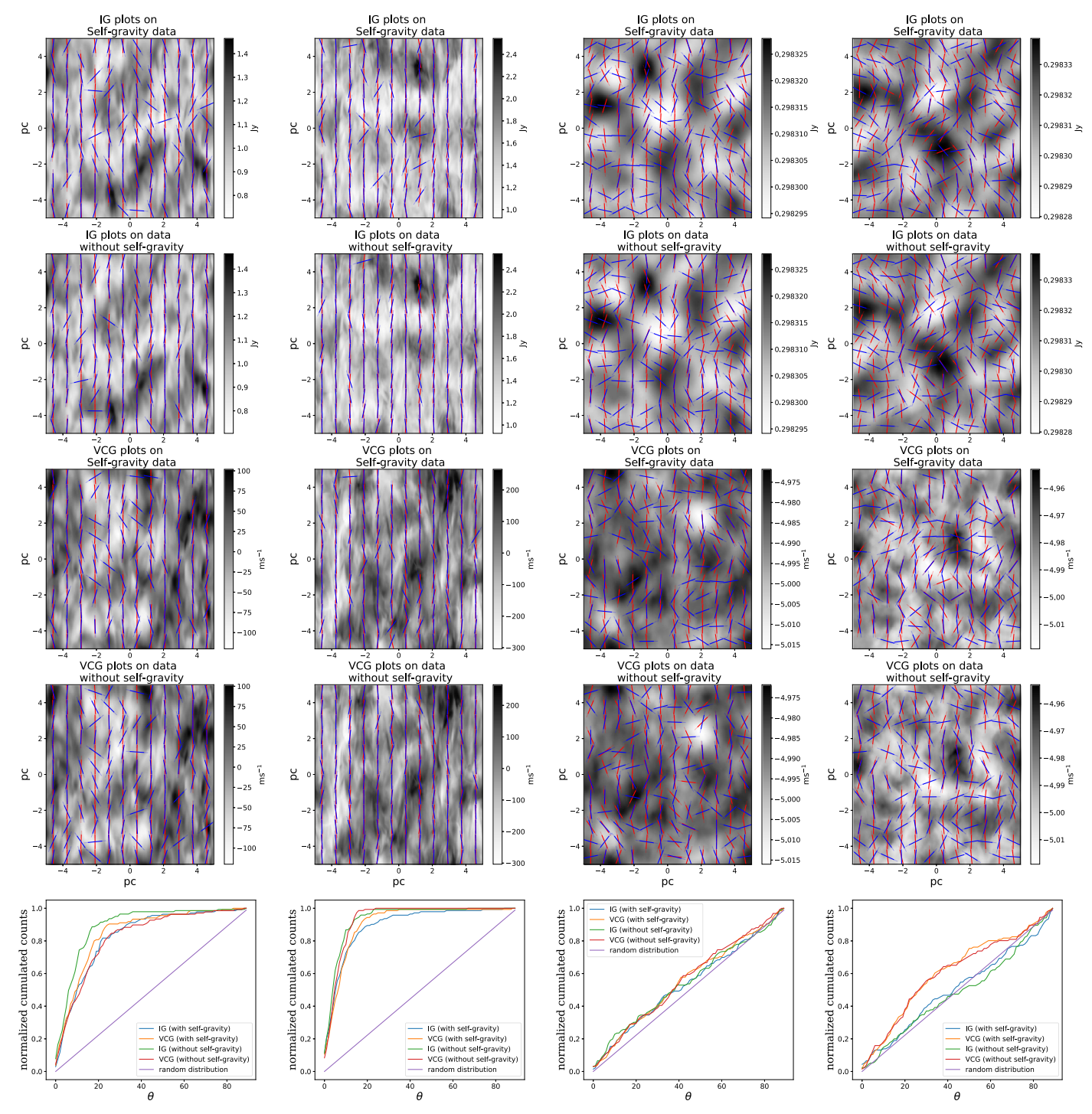


Figure 9. From left to right: b12 ($M_S = 0.92$, $M_A = 0.09$), b13 ($M_S = 1.95$, $M_A = 0.18$), b51 ($M_S = 0.05$, $M_A = 0.52$), and b52 ($M_S = 0.10$, $M_A = 1.08$) ¹³CO data sets. For each method (IGs and VCGs) and data set (with or without self-gravity), we plot the 2D vector plots and the statistical results. The blue vectors represent the projected B fields from the simulation, and the red vectors represent the VGT-predicted B-field direction. The relative angle between the simulated B field and the VGT-predicted direction is shown in the normalized cumulative plots.

Appendix C C¹⁸O Cumulative Plots

We plot the $C^{18}O$ results for models b12, b13, b51, and b52 in Figure 10. $C^{18}O$ shows similar results for the 4 models as

compared with ^{12}CO and C^{13}O . The major difference between the tracers is C^{18}O has a larger dispersion in the relative angle as compared to the other two tracers.

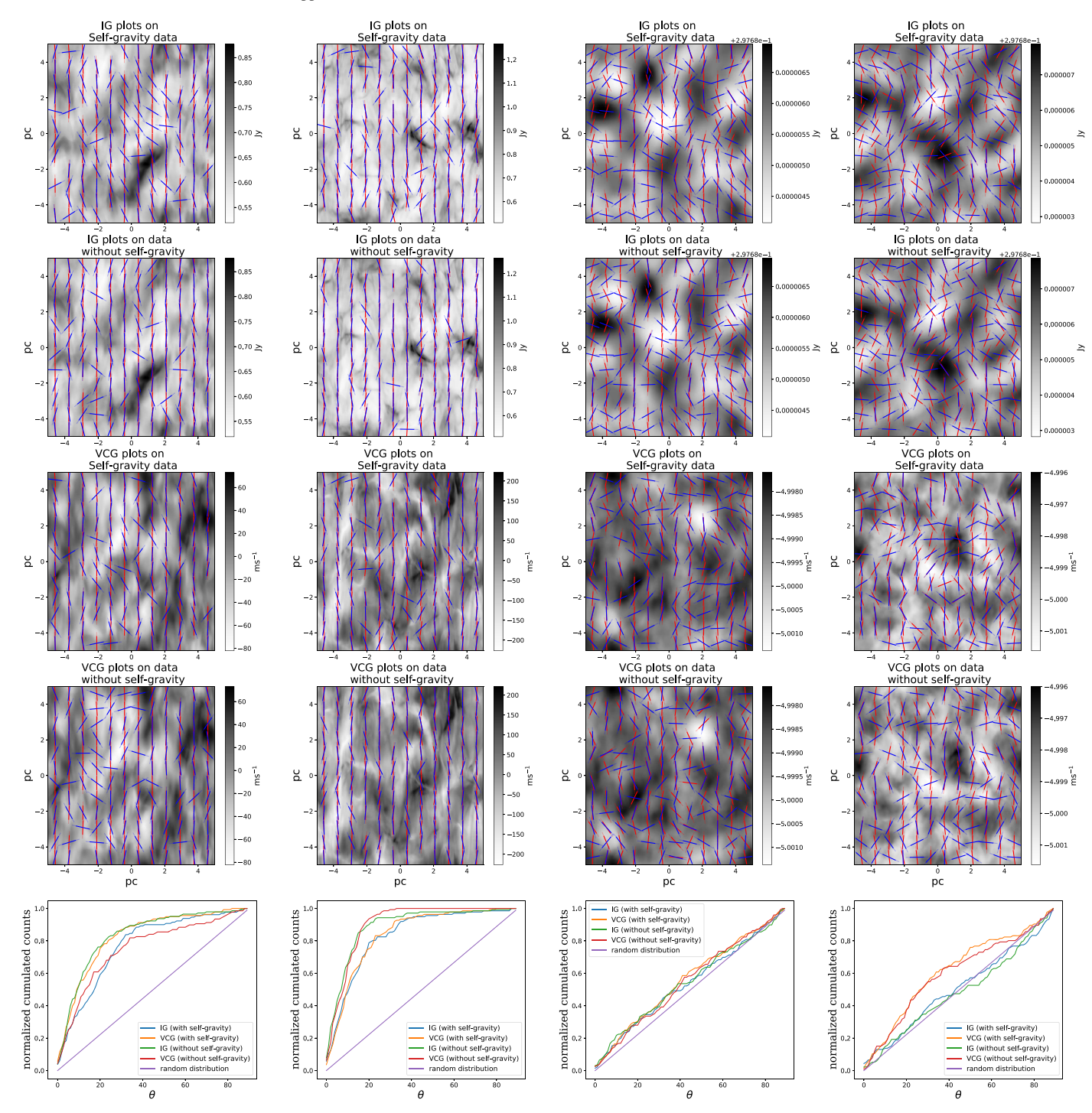


Figure 10. From left to right: b12 ($M_S = 0.92$, $M_A = 0.09$), b13 ($M_S = 1.95$, $M_A = 0.18$), b51 ($M_S = 0.05$), and b52 ($M_S = 0.10$, $M_A = 1.08$) C¹⁸O data sets. For each method (IGs and VCGs) and data set (with or without self-gravity), we plot the 2D vector plots and the statistical results. The blue vectors represent the projected B fields from the simulation, and the red vectors represent the VGT-predicted B-field direction. The relative angle between the simulated B field and the VGT-predicted direction is shown in the normalized cumulative plots.

ORCID iDs

Shih-Ping Lai https://orcid.org/0000-0001-5522-486X Sheng-Yuan Liu https://orcid.org/0000-0003-4603-7119

References

```
Andersson, B.-G., Lazarian, A., & Vaillancourt, J. E. 2015, ARA&A, 53,
Audit, E., & Hennebelle, P. 2005, A&A, 433, 1
Bodenheimer, P. H. 2011, in Principles of Star Formation, ed.
   P. H. Bodenheimer (Berlin: Springer)
Burn, B. J. 1966, MNRAS, 133, 67
Chandrasekhar, S., & Fermi, E. 1953, ApJ, 118, 113
Cho, J., & Lazarian, A. 2003, MNRAS, 345, 325
Cho, J., Lazarian, A., & Vishniac, E. T. 2002, ApJ, 564, 291
Cho, J., & Vishniac, E. T. 2000, ApJ, 539, 273
Crutcher, R. M. 2012, ARA&A, 50, 29
Crutcher, R. M., & Troland, T. H. 2008, ApJ, 685, 281
Crutcher, R. M., Wandelt, B., Heiles, C., Falgarone, E., & Troland, T. H. 2010,
   ApJ, 725, 466
Davis, L. 1951, PhRv, 81, 890
Elmegreen, B. G. 2000, ApJ, 530, 277
Eyink, G., Vishniac, E., Lalescu, C., et al. 2013, Natur, 497, 466
Eyink, G. L., Lazarian, A., & Vishniac, E. T. 2011, ApJ, 743, 51
Falceta-Gonçalves, D., Lazarian, A., & Kowal, G. 2008, ApJ, 679, 537
Falgarone, E., & Passot, T. 2003, LNP, 614, 3
Fissel, L. M., Ade, P. A. R., Angilè, F. E., et al. 2010, Proc. SPIE, 7741, 77410E
Fissel, L. M., Ade, P. A. R., Angilè, F. E., et al. 2016, ApJ, 824, 134
Goldreich, P., & Sridhar, S. 1995, ApJ, 438, 763
González-Casanova, D. F., & Lazarian, A. 2017, ApJ, 835, 41
Gonzalez-Casanova, D. F., & Lazarian, A. 2018, ApJ, submitted, (arXiv:1805.
González-Casanova, D. F., Lazarian, A., & Burkhart, B. 2017, ApJ, submitted,
```

(arXiv:1703.03035)

```
Hayes, J. C., Norman, M. L., Fiedler, R. A., et al. 2006, ApJS, 165, 188
Heiles, C. 2000, AJ, 119, 923
Hu, Y., Yuen, K. H., & Lazarian, A. 2018a, MNRAS, 480, 1333
Hu, Y., Yuen, K. H., Lazarian, V., et al. 2018b, NatAs, Submitted
Jijina, J., Myers, P. C., & Adams, F. C. 1999, ApJS, 125, 161
Larson, R. B. 1981, MNRAS, 194, 809
Lazarian, A. 2007, JOSRT, 106, 225
Lazarian, A., & Pogosyan, D. 2000, ApJ, 537, 720
Lazarian, A., & Vishniac, E. T. 1999, ApJ, 517, 700
Lazarian, A., Vlahos, L., Kowal, G., et al. 2012, SSRv, 173, 557
Lazarian, A., & Yuen, K. H. 2018a, ApJ, 865, 59
Lazarian, A., & Yuen, K. H. 2018b, ApJ, 853, 96
Lazarian, A., Yuen, K. H., Ho, K. W., et al. 2018, ApJ, 865, 46
Lazarian, A., Yuen, K. H., Lee, H., & Cho, J. 2017, ApJ, 855, 72
Mac Low, M.-M., & Klessen, R. S. 2004, RvMP, 76, 125
Maron, J., & Goldreich, P. 2001, ApJ, 554, 1175
McKee, C. F., & Ostriker, J. P. 1977, ApJ, 218, 148
Offner, S. S. R., Klein, R. I., & McKee, C. F. 2008, ApJ, 686, 1174
Soler, J. D., & Hennebelle, P. 2017, A&A, 607, A2
Soler, J. D., Hennebelle, P., Martin, P. G., et al. 2013, ApJ, 774, 128
Swift, J. J., & Welch, W. J. 2008, ApJS, 174, 202
Troland, T. H., & Crutcher, R. M. 2008, ApJ, 680, 457
van Dishoeck, E. F., Glassgold, A. E., Guélin, M., et al. 1992, in IAU Symp.
   150, Astrochemistry of Cosmic Phenomena, ed. P. D. Singh (Cambridge:
   Cambridge Univ. Press), 285
van Zadelhoff, G.-J., Dullemond, C. P., van der Tak, F. F. S., et al. 2002, A&A,
   395, 373
Wilson, C. D., Walker, C. E., & Thornley, M. D. 1997, ApJ, 483, 210
Wilson, T., Rohlfs, K., & Huettemeister, S. 2016, Tools of Radio Astronomy,
   Vol. 62 (Berlin: Springer)
Wilson, T. L. 1999, RPPh, 62, 143
Xu, S., & Lazarian, A. 2018, arXiv:1802.00987
Yuen, K. H., & Lazarian, A. 2017a, ApJL, 837, L24
Yuen, K. H., & Lazarian, A. 2017b, ApJ, submitted, (arXiv:1703.03026)
Yuen, K. H., Lazarian, V., & Lazarian, A. 2018, ApJ, submitted, (arXiv:1802.
   00024)
```